Monomeric Yeast Frataxin Is an Iron-Binding Protein†

Jeremy D. Cook,‡ Krisztina Z. Bencze,‡ Ana D. Jankovic,§ Anna K. Crater,‡ Courtney N. Busch,‡ Patrick B. Bradley,‡ Ann J. Stemmler,‡ Mark R. Spaller,§ and Timothy L. Stemmler*,‡

Department of Biochemistry and Molecular Biology, Wayne State University, School of Medicine, 540 East Canfield Avenue, Detroit, Michigan 48201, and Department of Chemistry, Wayne State University, 5101 Cass Avenue, Detroit, Michigan 48202

Received March 3, 2006; Revised Manuscript Received April 24, 2006

ABSTRACT: Friedreich's ataxia, an autosomal cardio- and neurodegenerative disorder that affects 1 in 50 000 humans, is caused by decreased levels of the protein frataxin. Although frataxin is nuclear-encoded, it is targeted to the mitochondrial matrix and necessary for proper regulation of cellular iron homeostasis. Frataxin is required for the cellular production of both heme and iron−sulfur (Fe−S) clusters. Monomeric frataxin binds with high affinity to ferrochelatase, the enzyme involved in iron insertion into porphyrin during heme production. Monomeric frataxin also binds to Isu, the scaffold protein required for assembly of Fe−S cluster intermediates. These processes (heme and Fe−S cluster assembly) share requirements for iron, suggesting that monomeric frataxin might function as the common iron donor. To provide a molecular basis to better understand frataxin's function, we have characterized the binding properties and metal-site structure of ferrous iron bound to monomeric yeast frataxin. Yeast frataxin is stable as an iron-loaded monomer, and the protein can bind two ferrous iron atoms with micromolar binding affinity. Frataxin amino acids affected by the presence of iron are localized within conserved acidic patches located on the surfaces of both helix-1 and strand-1. Under anaerobic conditions, bound metal is stable in the high-spin ferrous state. The metal−ligand coordination geometry of both metal-binding sites is consistent with a six-coordinate iron−(oxygen/nitrogen) based ligand geometry, surely constructed in part from carboxylate and possibly imidazole side chains coming from residues within these conserved acidic patches on the protein. On the basis of our results, we have developed a model for how we believe yeast frataxin interacts with iron.

Friedreich's ataxia (FRDA) is an autosomal recessive cardio- and neurodegenerative disorder that affects approximately 1 in 50 000 people (*1*−*3*). The disorder, in the majority of FRDA patients, is a direct result of a trinucleotide repeat expansion in the first intron of the gene for the protein frataxin; this expansion disrupts gene transcription, leading to a frataxin deficiency in humans (*4*). The inability to produce frataxin is associated with mitochondrial accumulation of iron that is biologically unavailable. In humans, the breakdown in normal iron regulation pathways resulting from frataxin deficiency is exemplified physiologically by the degeneration of sensory neurons in the dorsal root ganglia, hypertrophic cardiomyopathy, and diabetes mellitus (*5*). In yeast, reintroduction of frataxin into knockout cells results in restored bioavailability of the accumulated metal (*6*). These data indicate that frataxin is required for retaining bioavailable iron within the mitochondria.

While the exact function of frataxin regarding mitochondrial iron homeostasis is unclear, numerous reports have suggested that the protein participates in various facets of iron metabolism. Frataxin was initially suggested to act as a facilitator or regulator of mitochondrial iron export; thus, the loss of function is associated with mitochondrial iron accumulation (*6*). Frataxin has been implicated in energy conversion and ATP synthesis (*7*) and in protecting aconitase $[4Fe-4S]^{2+}$ clusters against disassembly and inactivation (*8*, *9*). Frataxin has been shown to form spherical in vitro homo-oligomers under low salt and high iron concentrations, suggesting a possible iron storage capacity for the protein (*10*−*13*). Finally, frataxin has been shown to be involved in the in vivo production of both heme (*14*−*16*) and Fe−S clusters (*17*−*21*). Monomeric frataxin binds with nanomolar-binding affinity to the ferrochelatase and ISU assembly apparatus enzymes responsible for respective heme and Fe−S cluster production (*14*, *17*, *22*, *23*). Activity assays reported using in vitro protein show that monomeric human frataxin stimulates production of heme and Fe−S clusters (*22*, *23*). Similar in vitro heme assembly activity was reported for yeast frataxin oligomers (*24*); however, a recent paper indicates yeast frataxin mutants with diminished assembly capability are also active for in vitro heme assembly (*25*). In vivo studies have also shown that yeast cells containing frataxin mutants that lack the self-assembly ability have normal phenotypes with regard to Fe−cofactor production (*26*). These data suggest that the monomeric form of frataxin

† This work was supported by the American Heart Association, Midwest Affiliate to T.L.S. (0130527Z) and by the National Institutes of Health to T.L.S. (DK068139).

* To whom correspondence should be addressed: Department of Biochemistry and Molecular Biology, Wayne State University, School of Medicine, 540 E. Canfield Ave., Detroit, MI 48201. Telephone: 313-577-5712. Fax: 313-577-2765. E-mail: tstemmle@med.wayne.edu.

‡ Department of Biochemistry and Molecular Biology.

§ Department of Chemistry.

10.1021/bi060424r CCC: $33.50
Published on Web 05/28/2006

controls iron delivery during both heme and Fe−S cluster assembly.

The amino acid sequence and structure of frataxin orthologues are both well-conserved and provide insight into where the protein may bind iron. Frataxin orthologues share a general sequence homology (ca. 60%) specifically with regards to conserved acidic residues (*27*). Structures of the yeast, human, and bacterial orthologues show that frataxin is a member of the α−*β* sandwich motif family, constructed predominately by two parallel α helices on the helical plane and five antiparallel *β* strands on the *β*-sheet protein surface of the protein (*28*−*32*). The highly conserved aspartic and glutamic acid residues line the exposed planer edge of the protein at the N-terminal α helix (helix-1) and *β* strand (strand-1) interface. Nuclear magnetic resonance (NMR)[1] analyses indicate that chemical environments of these conserved acidic residues are perturbed when iron is present (*28*, *32*). A subset of these conserved acidic residues are responsible for the iron-induced assembly and ferroxidase activities reported for in vitro frataxin (*25*−*27*). A common theme in iron-binding metalloproteins is the use of carboxylate oxygen and imidazole nitrogen atoms, from Asp, Glu, and His protein side chains, acting as direct ligands to bind metal (*33*−*35*). Given the high conservation of Asp and Glu residues in this protein region, the fact that these residues are directly affected by the presence of iron, and because specific residues in these regions have been shown to be required for iron regulation, it seems likely these acidic residues are directly utilized by frataxin during iron binding.

The goal of this paper is to provide additional structural and biochemical detail to better understand how frataxin binds iron. Although our studies were performed solely on yeast frataxin homologue 1 protein (Yfh1), given the high sequence homology and structural similarities between protein family members, these results provide additional direct insight into general properties that dictate how frataxin orthologues bind iron. We made specific emphasis to characterize the iron-binding ability of the monomeric form of yeast frataxin because of the mounting evidence that it is the monomeric protein that interacts with protein partners during iron−cofactor assembly. Papers showing that oligomeric frataxin assists in controlling oxidative stress are also certainly convincing, indicating that frataxin aggregates may regulate reactive oxygen species availability and/or iron-induced cellular damage under oxidative-stress conditions. While the iron-loaded yeast frataxin trimer has been speculated as being the nucleating species in higher-order oligomer formation by the protein (*12*), we would argue that the first step in oligomer assembly in fact involves the interaction between monomeric frataxin and iron. A direct structural understanding of how monomeric frataxin interacts with iron would therefore also provide insight into the participation of the protein in early mechanistic steps during control of cellular iron bioavailability. Solution conditions shown to promote stable iron-loaded yeast frataxin monomers have been published, and these conditions were utilized within this study (*27*). Thermodynamic analyses were used to measure the iron-binding affinity and metal/protein stoichiometry of yeast frataxin. NMR spectroscopic analysis was used to further identify amino acids affected by the presence of iron. Finally, X-ray absorption spectroscopic (XAS) studies were used to determine the oxidation and spin state of iron bound to frataxin, as well as help provide structural detail regarding how monomeric frataxin binds iron.

[1] Abbreviations: Yfh1, yeast frataxin homologue 1 protein; NMR, nuclear magnetic resonance; XAS, X-ray absorption spectroscopy; XANES, X-ray absorption near edge structure; EXAFS, extended X-ray absorption fine structure; ITC, isothermal titration calorimetry; ICP−MS, inductively coupled plasma−mass spectroscopy.

MATERIALS AND METHODS

Protein Expression and Isolation. The mature full-length yeast frataxin coding sequence, representing residues 52−174 of the complete open-reading frame, with a Met substituting the Val at position 52, was subcloned into a pET11a bacterial expression vector (Novagen). The growth and isolation strategy for preparing homogeneous yeast frataxin was previously described in detail (*28*). Unlabeled and ^{15}N-labeled protein were expressed in *Escherichia coli* BL21(DE3) cells grown at 37 °C in Luria−Bertani media (unlabeled protein) or M9 minimal media containing $^{15}NH_4Cl$ (^{15}N-labeled protein). Protein expression was induced with 1 mM isopropyl-*β*-D-thiogalactopyranoside (IPTG), and cells were grown post-induction for 4 h prior to isolation. Cells were harvested by centrifugation, lysed with a French press, sonicated, and finally spun at high speed (18 000 rpm) for 1 h. Two ammonium sulfate precipitation steps were used to obtain a partially purified frataxin pellet. Solubilized protein was run on anion-exchange and phenyl-sepharose columns, each with salt gradients, to obtain pure protein. Average yields amount to 70 and 30 mg/L of pure unlabeled and labeled protein, respectively. Newly isolated protein was stored under an oxygen-depleted argon atmosphere at 4 °C in 20 mM HEPES (pH 7.0) and 10 mM $MgSO_4$. Apo-Yfh1 is susceptible to auto-aggregation in a time-dependent manner (data not shown), and under these solution conditions, monomeric yeast frataxin was stable for only up to 2 weeks. As a result, all of our experiments were performed on protein obtained within a 2 week window after isolation.

Size-Exclusion Chromatography/Inductively Coupled Plasma−Mass Spectroscopy (ICP−MS) Analysis. Size-exclusion chromatography and ICP−MS studies were used to confirm the solution conditions under which iron-loaded yeast frataxin was stable as a monomer. Protein samples were prepared anaerobically in 20 mM HEPES buffer (pH 7.0) and 10 mM $MgSO_4$. Iron-loaded frataxin samples at 1:1 and 2:1 Fe^{II}/protein stoichiometries were prepared anaerobically by combining concentrated solutions of buffered protein and buffered ferrous ammonium sulfate (Sigma). All solutions were initially made anaerobic by repeated cycles of vacuum and argon(g) purging on a Schlenk line; samples were capped using septa on all glassware. Samples were mixed within a nitrogen(g)-filled glovebox (Plas Labs, Lansing, MI) to form the iron−protein complexes. Samples were loaded, using an anaerobic syringe, onto a 1.2 m long Sephacryl S-200 or a 2 m long Sephacryl S-100 high-resolution size-exclusion column, both attached to a BioRAD BioLOGIC *LP* system. An argon-purged buffer solution of 20 mM HEPES (pH 7.0) and 10 mM $MgSO_4$ was used, first to equilibrate and wash the column and then as our running buffer. The column was run at room temperature. A protein control sample (BioRad) of buffered vitamin B_{12} (1.3 kDa), myoglobin (17 kDa),

ovalbumin (44 kDa), γ globulin (158 kDa), and thyroglobulin (670 kDa) was used to calibrate the molecular size.

ICP−MS analysis was performed on a PE Sciex Elan 9000 spectrometer equipped with a cross-flow nebulizer and Scott-type spray chamber. The RF power was held at 1000 W, and argon gas flow was optimized at 0.9 L/min. The optimum lens voltage was centered on rhodium sensitivity as counts per second. Samples were prepared by treatment with nitric acid and heated at 70 °C for 1 h to digest the protein. Final samples were diluted with iron-free HPLC-grade water. A calibration curve, obtained from diluted stock solutions of 1000 ppm ferrous standards in 2% HNO_3 (high-purity acid, OmniTrace EM Science), was used to correlate protein-bound iron to known metal concentrations. All results are determined from three replicate experiments performed on at least two different but independent protein sample preparations.

Isothermal Titration Calorimetry (ITC). ITC measurements were performed to determine the metal-binding affinity and maximum metal/protein stoichiometry of monomeric yeast frataxin. Experiments were conducted at 30 °C on a VP−ITC titration microcalorimeter (MicroCal, Inc.). Protein and aqueous ferrous ammonium sulfate solutions were prepared anaerobically in 20 mM HEPES (pH 7.0) and 10 mM $MgSO_4$. Experiments were designed to keep a ca. 20-fold excess of iron in the syringe, and data were collected at three independent protein concentrations (100, 70, and 50 μM) corresponding to aqueous iron solutions of 2.5, 1.4, and 0.8 mM, respectively. Protein samples were loaded anaerobically into the sample chamber, and after an initial 2 μL iron solution injection, 29 additional injections of 10 μL each were titrated into the protein sample. Spacing between injections was 10 min, and the stirring speed of the syringe was held constant at 500 rpm. All experiments were repeated in triplicate on independent protein and iron samples to ensure data reproducibility. The Origin 5.0 software package supplied by MicroCal, Inc. was used for data analysis. Origin 5.0 uses a nonlinear least-squares curve-fitting algorithm to determine the stoichiometric ratio, dissociation constant, and change in enthalpy of the reaction.

NMR Iron Titration. NMR amide chemical-shift perturbation experiments were used to identify amino acids affected by the presence of iron under solution conditions that stabilize monomeric iron-loaded frataxin. Spectra were collected on a Varian INOVA 600 MHz spectrometer equipped with a triple-resonance $^1H/^{13}C/^{15}N$ Varian cold probe with *z*-axis-pulsed field gradients. Aqueous anaerobic concentrated ferrous ammonium sulfate (Sigma) was titrated into an anaerobic solution of ^{15}N-labeled yeast frataxin (protein concentration of ca. 1 mM) to achieve Fe^{II}−protein stoichiometric ratios of 1 and 2. Samples were prepared in 20 mM HEPES buffer (pH 7.0) and 10 mM $MgSO_4$ buffer at room temperature under an Ar(g) atmosphere. Samples were anaerobically transferred into septa-sealed 5 mm NMR tubes using airtight transfer syringes. Protein samples were placed in the NMR spectrometer and allowed to equilibrate at 30 °C for 30 min. Full $^1H/^{15}N$ heteronuclear single-quantum coherence (HSQC) spectra were collected at each titration point with a ^1H sweep width of 9000.9 Hz, with 2048 points and 32 transients, and at a ^{15}N sweep width of 2500 Hz, 512 increments (*36*). Full independent spectra were collected on at least two samples to ensure spectral reproducibility. Chemical shifts were referenced using an external DSS control sample (*37*). Data were transformed using NMRPipe (*38*), and amide chemical shifts were identified/measured using SPARKY (*39*). Protein amide resonances that were significantly line-broadened by the presence of ferrous iron were identified first. Amide proton and nitrogen chemical shifts were measured for the remaining residues. Amide chemical-shift changes were calculated and normalized to obtain a chemical-shift change (δ) value for each spectral pair using the equation $\delta = 25((\delta_{HN})^2 + (\delta_N/5)^2)^{0.5}$ (*40*).

XAS Sample Preparation and Analysis. XAS was used to study the electronic properties and ligand coordination geometry of iron bound to frataxin. All samples were prepared anaerobically within a glovebox using protein and iron solutions that were initially prepared on a Schlenk line and then stored under an Ar(g) atmosphere. XAS samples were prepared at 1 mM protein concentrations in 20 mM HEPES buffer (pH 7.0) and 10 mM $MgSO_4$ and mixed with buffered anaerobic ferrous aqueous iron in the same manner outlined above. Samples were concentrated to 2 mM iron concentrations using centricon 10 kDa cutoff membranes and diluted to 30% glycerol as a glassing agent. Samples were loaded into Lucite cells wrapped with Kapton tape, flash-frozen in liquid nitrogen, removed from the glovebox, and stored in liquid nitrogen until used. Solid model samples of $Fe(NH_4)_2(SO_4)_2{\cdot}(H_2O)_6$, FeS, $Fe_2(SO_4)_3$, Fe_2O_3, $FeCl_3$ (all from Sigma), and $Fe(imidazole)_6$ [prepared in our laboratory (*41*)] were used as controls for calibrating our protein XAS data analysis. Model samples were diluted with boron nitride in a glovebox, loaded directly in Kapton tape-wrapped aluminum transmission cells, and flash-frozen in liquid nitrogen upon removal from the glovebox. At least two independent samples were made for each protein and model sample to ensure data reproducibility.

XAS data were collected at the Stanford Synchrotron Radiation Laboratory (SSRL), beamlines 7-3 and 10-2, and at the National Synchrotron Light Source (NSLS), beamline X9-b. Both SSRL beamlines were equipped with Si(220) double-crystal monochromators detuned 50% for harmonic rejection. NSLS beamline X9-b was equipped with a Si(111) single-crystal monochromator equipped with a harmonic rejection mirror. Samples were maintained at 10 K using Oxford Instruments continuous-flow liquid helium cryostats at SSRL and at ca. 24 K using a He Displex Cryostat at NSLS. Protein fluorescence excitation spectra were collected using 30-element Ge solid-state array detectors at SSRL and a 13-element Ge solid-state detector at NSLS. Transmission data were recorded on model compounds using ionization detectors filled with nitrogen gas, placed before and after the cryostat. XAS spectra were measured using 5 eV steps in the pre-edge regions (6900−7094), 0.25 eV steps in the edge regions (7095−7135 eV), and 0.05 $Å^{-1}$ increments in the extended X-ray absorption fine structure (EXAFS) region (to $k = 13.5$ $Å^{-1}$), integrating from 1 to 20 s in a k^3-weighted manner for a total scan length of approximately 40 min. X-ray energies were calibrated by collecting an iron-foil absorption spectrum simultaneously with the collection of the protein and model data. The first inflection point for the Fe-foil edge was assigned at 7111.3 eV. Each fluorescence channel of each scan was examined for spectral anomalies prior to averaging, and spectra were closely monitored for photoreduction. SSRL protein data represent the average of

5−6 scans, while NSLS protein data represent the average of 8−9 scans.

XAS data were processed using the Macintosh OS X version of the EXAFSPAK program suite integrated with the Feff version 7.2 software for theoretical model generation (*42*, *43*). XAS data reduction utilized a Gaussian function in the pre-edge region and a three-region cubic spline in the EXAFS region. EXAFS data were converted to *k* space using an E_0 value of 7130 eV. The *k*-cubed weighted EXAFS was truncated at 1.0 and 12.85 $Å^{-1}$ for filtering purposes and Fourier-transformed. Data were Fourier-filtered to isolate the EXAFS for each peak in the Fourier transform and then fit. The final published fitting results are from analysis of the raw unfiltered data.

Analysis of the X-ray absorption near edge structure (XANES) 1s → 3d transitions was completed using the EDG_FIT subroutine within EXAFSPAK (*43*). Only spectra collected using the higher resolution [Si220] monochromator crystals were subjected to edge analysis. Pre- and post-transition splines were fit to the spectra within the energy range of 7090−7100 and 7120−7125 eV, respectively. The extrapolated line was then subtracted from raw data to obtain baseline-corrected spectra. The pre-edge features were modeled using pseudo-Voigt line shapes (simple sums of Lorentzian and Gaussian functions), and the energy position, the full width at half-maximum (fwhm), and the peak heights for each transition were varied. A fixed 50:50 ratio of Lorentzian/Gaussian functions successfully reproduced the spectral features of the pre-edge transitions. Global peak transition areas were determined for all spectra over the energy range of 7109−7117 eV using Kaleidagraph. Pre-edge intensity values were multiplied by 100 to match the published procedure, and area values shown for our models are nearly identical to published values (*44*).

EXAFS data-fitting analysis performed on both Fourier filtered and raw/unfiltered data gave equivalent structural results. Model and protein EXAFS data were fit using both single- and multiple-scattering amplitude and phase functions calculated using Feff version 7. Single-scattering Feff version 7 models were calculated for carbon, oxygen, sulfur, and iron coordination to simulate possible iron−ligand environments in our systems. Multiple-scattering Feff version 7 models were generated for iron−imidazole interactions utilizing crystallographic coordinates from characterized model compounds. Fits to the crystallographically characterized model compounds were used to calibrate the scale factor, and ΔE_0 values were used in our protein fits. A scale factor of 0.95 and a threshold shift (ΔE_0) of −11.5 eV were used during our protein data analysis. The scale factor and E_0 were not allowed to vary because they were calibrated from the Fe^{II} model compounds matching the oxidation state of the ferrous iron that we found in our protein samples. When empirical data were simulated, metal−ligand coordination numbers were fixed at half-integer values, while only the absorber−scatterer bond length (*R*) and Debye−Waller factor (σ^2) were allowed to freely vary. The criteria for judging the best fit simulation and for adding ligand environments to the fit included (A) the lowest mean-square deviation between data and fit (F'), a value corrected for the number of degrees of freedom in the fit, (B) individual shell-bond distances that must be outside the spectral resolution (>0.13 Å), and finally, (C) all Debye−Waller factors in the ligand system that must have values less than 0.006 $Å^2$ (*35*, *45*).

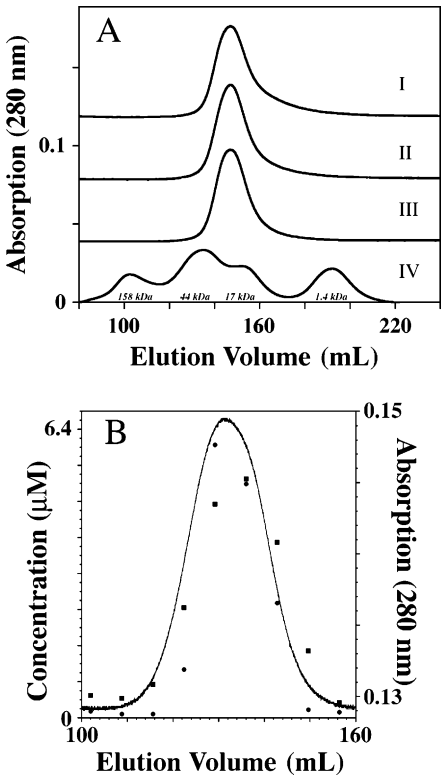

FIGURE 1: Oligomeric state and iron−protein stoichiometry for yeast frataxin samples. (A) Size-exclusion chromatographs for yeast frataxin with 2, 1, or 0 iron atoms bound shown in (I), (II), and (III) respectively, coupled with protein standards (IV). Samples were run anaerobically on a S-200 Sephacryl size-exclusion column at 27 °C. (B) Representative comparison of the ICP−MS iron quantitation (■) versus the protein concentration from a Bradford assay (●) for 1:1 iron-loaded yeast frataxin on data collected on a high-resolution S-100 Sephacryl column under identical conditions as when we ran the S-200 column.

RESULTS

Iron-Loaded Yeast Frataxin Is a Stable Monomer. To characterize the in vitro iron-binding properties of monomeric yeast frataxin, we employed solution conditions that stabilize monomeric iron-bound yeast frataxin (*27*). The presence of magnesium or calcium salts stabilize iron-loaded monomeric yeast frataxin, and the absence of oxygen helps to stabilize iron bound to frataxin in the ferrous oxidation state. We prepared frataxin samples anaerobically with zero, one, and two iron bound per monomer in 20 mM HEPES buffer (pH 7.0) in the presence of 10 mM $MgSO_4$. Samples were subjected to size-exclusion chromatography to ensure that protein with the bound iron was stable as a monomer.

Under these solution conditions, apo-yeast frataxin elutes from the sizing column as a single band, consistent with the apoprotein existing as a stable monomer (Figure 1A, III). Full-length mature apo-yeast frataxin (123 amino acids) consistently runs at ca. 17 kDa on sizing columns. Protein samples were characterized by mass spectrometry to ensure no degradation was taking place following extensive exposure to iron. Surprisingly, in vitro isolated apoprotein was susceptible to homo-oligomerization in progressively increasing amounts, in a buffer- and iron-independent fashion, after about 2 weeks post-isolation (data not shown). As a

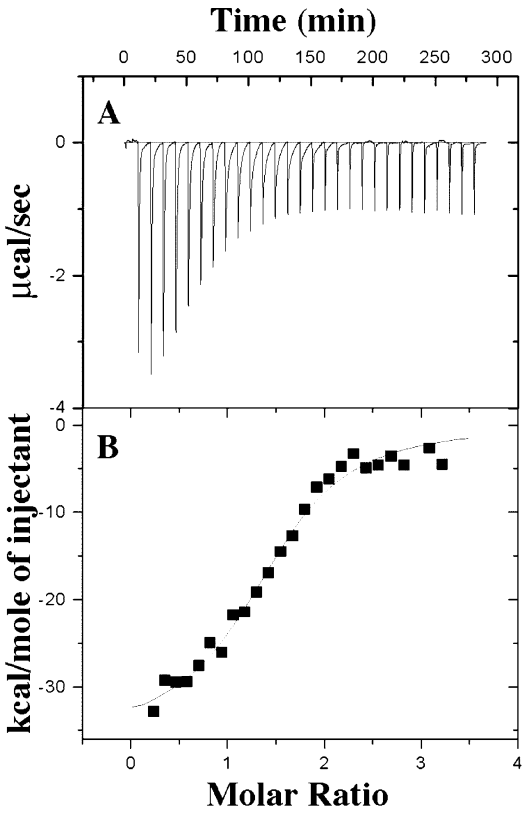

FIGURE 2: Raw ITC (A) and binding isotherm data (B) for ferrous iron to yeast frataxin. The gray line in A shows the baseline, and the gray line in B shows the simulated fit to the binding isotherm data. Data were collected anaerobically at 30° in 20 mM HEPES (pH 7.0) and 10 mM $MgSO_4$. These data were collected by injecting small aliquots of a 0.8 mM ferrous iron solution into a 50 μM Yfh1 sample. Spacing between injections was 10 min. Syringe-stirring speed was kept at 500 rpm.

result, all experiments were performed immediately (or up to 2 weeks) after the protein was isolated. The protein was stored anaerobically at 4 °C when not in use and discarded after 2 weeks. The addition of ferrous iron at either a 1:1 or 2:1 metal/protein stoichiometric ratio had no effect on the oligomeric state of the protein under these solution conditions (II and I in Figure 1A, respectively). In each case, the protein elutes from the column at the same position as the monomeric apofrataxin band in the chromatograph. ICP−MS analysis coupled to a Bradford assay was used to confirm that the metal is still bound to the protein following separation (Figure 1B).

Yeast Frataxin Binds Two Iron Atoms at Micromolar Affinity. ITC was used to provide insight into the iron-binding affinity of the monomeric yeast frataxin and the maximal number of ferrous iron atoms that the protein can bind. ITC measurements were performed anaerobically under solution conditions that stabilized the monomeric iron-loaded protein. Changes in heat resulting from iron binding are displayed in μcal/s on the raw ITC data (Figure 2A). These data show a single strong exothermic reaction that follows exponential behavior in the early injection points. Heats at the end of the titration equal those obtained from Fe^{II} alone, indicating that metal binding is complete following the early titration points. Initially, data sets were treated using a model with one set of binding sites (Origin 5.0). The calculated stoichiometry from the fitted curve provided for an average of 1.4−1.6 iron atoms per monomeric frataxin. However, upon analyzing the diagram, it was apparent that complete saturation is achieved for a 2:1 Fe^{II}/protein ratio. Considering also the nature of binding sites in yeast frataxin, an advanced curve fitting of two sets of binding sites was employed. The theoretical curve for this model resulted in a better fit to the original data represented in the metal-binding isotherm (Figure 2B) and used to determine the metal-binding affinity of the protein. After curve-fitting analysis, binding affinities for both sites was determined to be in the micromolar range ($K_{d_1} = 3.0 \pm 0.4$ μM and $K_{d_2} = 2.0 \pm 0.2$ μM). These results indicate that the two metal-binding sites are independent, although they have nearly identical binding affinities.

Mapping the Iron-Binding Surface of Yeast Frataxin. NMR spectroscopy was used to identify frataxin amino acids perturbed by the presence of ferrous iron under solution conditions that stabilize the monomeric protein. Our goal was to locate the region of the monomeric protein affected by the presence of iron with the intent to determine which amino acids may be directly involved in iron binding. We recently reported a similar titration on yeast frataxin in sodium phosphate buffer, corresponding to conditions that we utilized when solving the solution structure of the protein (*28*). However, we repeated these studies in HEPES/$MgSO_4$ buffer to confirm that the protein with metal bound was a stable monomer and also to provide a better representation of the iron-binding ability of frataxin under solution conditions similar to those seen in vivo that surely contain salt. Buffered anaerobic ferrous ammonium sulfate was added to anaerobic ^{15}N-labeled yeast frataxin at 1:1 and 2:1 metal/protein stoichiometries. ^{15}N-Filtered HSQC spectra were used to identify amide chemical-shift perturbations of residues affected by the presence of iron (*36*). As observed in our phosphate-buffered titration, residues localized within the helix-1 and strand-1 regions of frataxin were significantly perturbed by the presence of iron (Figure 3) (*28*). However, unlike our initial phosphate buffer results, a second set of residues underwent substantial amide line broadening in the iron-loaded spectra. Additional residues in the β-sheet and helix-2 regions were also affected in the presence of iron under these new buffer conditions. Residues with significant amide chemical-shift perturbations (i.e., greater than 2 times the resolution of the data) include E24, E25, D27, L33, S36, L37, E38, E39, L40, S41, E42, and A43 in helix-1, G56 in the strand-1/-2 connecting loop, K77 in the strand-3/-4 connecting loop, W80 in strand-4, and E116, A119, and K121 in helix-2. The second residue set, with amide resonance that was line-broadened beyond recognition, include D28, D31, H32, L33, and D35 in helix-1, E52 in strand-1, E61 in strand-2, T67 in strand-3, and Q123 at the C terminus. Residue numbers represent the sequence position corresponding to the mature processed protein.

Iron Coordination Geometry of Iron-Loaded Monomeric Frataxin. XAS studies were used to obtain an electronic and structural characterization of iron bound to monomeric yeast frataxin. Full XAS data sets were collected on multiple independent yeast frataxin samples with one iron (1Fe−Yfh1) and two iron (2Fe−Yfh1) bound. Samples were again prepared under solution conditions that stabilized the iron-bound protein monomer. XANES spectra for the different protein samples are compared to Fe^{II} and Fe^{III} controls in Figure 4. General edge features from the protein samples closely resemble those obtained from the ferrous ammonium

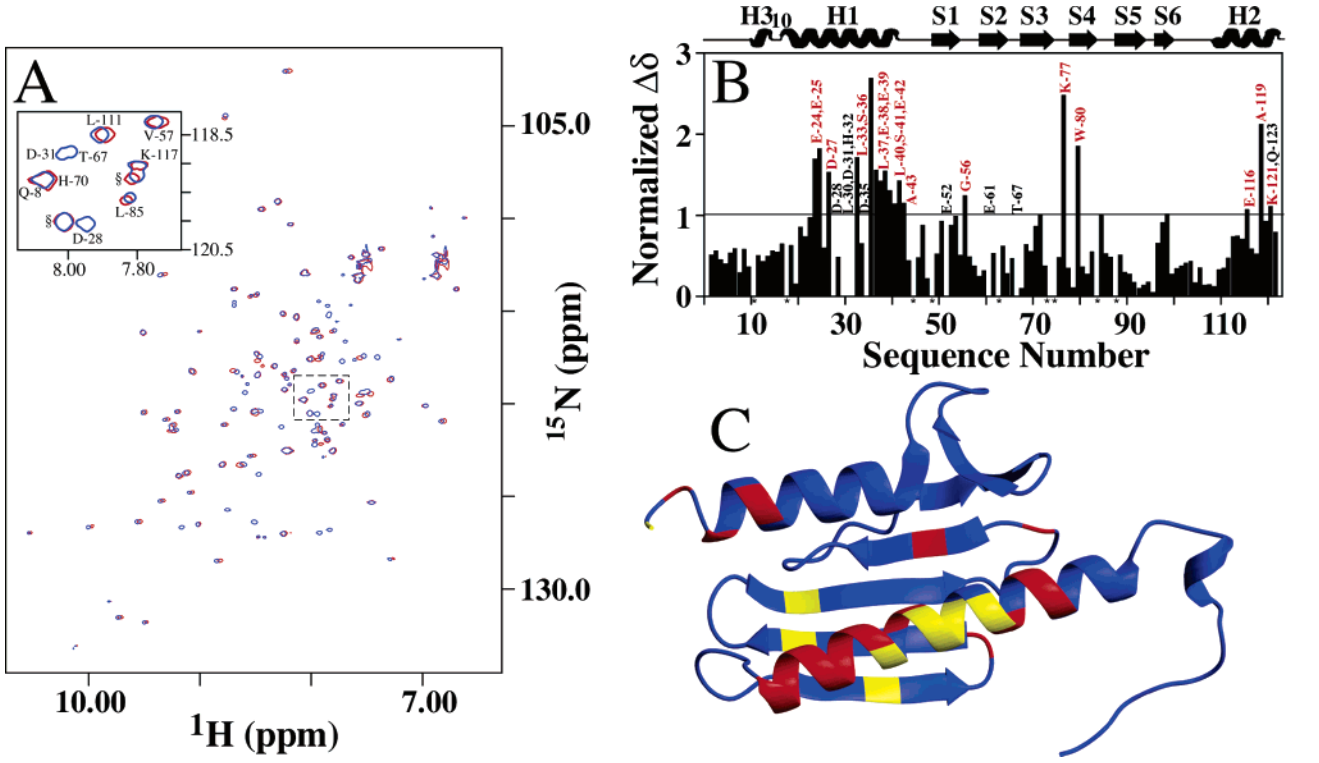

FIGURE 3: Frataxin residues perturbed at the amide position by the presence of iron. (A) ^{15}N-filtered HSQC spectra for 500 μM apo- (blue) and 2Fe−Yfh1 (red) in 20 mM HEPES buffer (pH 7.0) and 10 mM $MgSO_4$ at 600 MHz. NMR data collected anaerobically at 30 °C. (Inset) Expanded region marked in dashed lines with residues identified, "§" indicates side chain or unassigned peaks. (B) Summary of yeast frataxin-normalized amide chemical-shift changes in the presence and absence of 2 equiv of iron. Residues identified in black correspond to paramagnetically broadened amide signals. Residues identified in red correspond to amide signals with chemical-shift changes. Residues indicated with an asterisk in the *x* axis indicate Pro positions. A horizontal black line indicates a chemical-shift cutoff, which corresponds to 2× data resolution. (Top) Secondary-structural elements for yeast frataxin with helices and strands labeled as H and S, respectively. (C) Location of residues on apo-yeast frataxin structure with amide backbone resonances that are significantly line-broadened (yellow) or have substantial chemical-shift changes (red) in the presence of Fe^{II}. Note: the structure of the protein represents an updated PDB file for yeast frataxin (PDB accession number 2GA5), currently available for download.

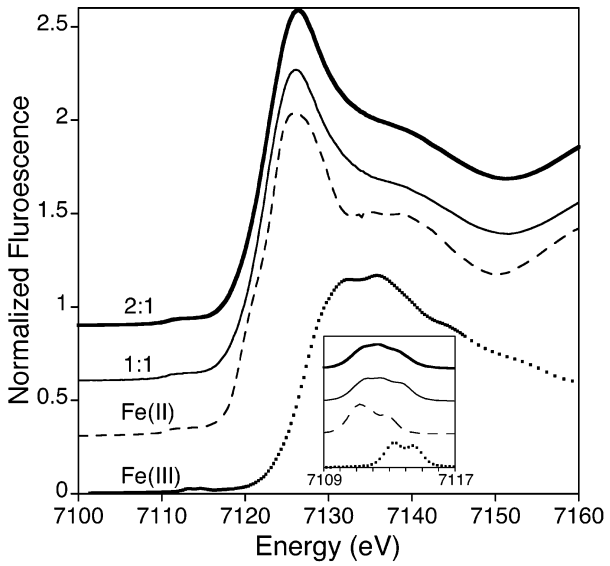

FIGURE 4: XANES comparison of iron−yeast frataxin with ferrous and ferric models. Full XANES spectra for yeast frataxin with one iron (—) and two iron bound (—) with ferrous ammonium sulfate (- - -) and ferric ammonium sulfate (···). (Inset) Expansion of the background-subtracted 1s → 3d region of the XANES spectra for all samples.

sulfate control spectrum (Figure 4A). The first inflection edge energies measured for 1Fe−Yfh1 and 2Fe−Yfh1 were at 7122.40 ± 0.02 and 7122.75 ± 0.03 eV, respectively. The averaged edge inflection energy for the two signals in our ferrous ammonium sulfate control occurs at 7122.90 ± 0.03 eV, while the first inflection energy for our ferric ammonium sulfate control occurs at 7126.30 ± 0.02 eV. Our protein edge inflection energies more closely resemble values seen for our ferrous control, indicating that bulk iron bound to monomeric yeast frataxin is predominately in the ferrous oxidation state. The pre-edge features, centered at ca. 7112 eV in the Fe^{II} containing XANES spectra, arise from the 1s → 3d electronic transitions in the XAS absorption edge (*44*, *46*−*48*). The 1s → 3d signals in the protein XANES spectra were compared to model spectra to identify the spin state and ligand symmetry of Fe^{II} bound to Yfh1. Three independent 1s → 3d transitions were measured for both 1Fe−Yfh1 and 2Fe−Yfh1 at 7111.27 ± 0.02, 7112.28 ± 0.03, and 7113.38 ± 0.02 eV. The global area for these transitions were measured in unitless values for both 1Fe−Yfh1 and 2Fe−Yfh1 at 5.46 ± 0.07 and 5.56 ± 0.01, respectively. A comparison of these spectral features to published iron model data indicate that ferrous iron bound to yeast frataxin is most likely high-spin, on the basis of the intensity, number, and energy of the observed transitions (*44*, *46*). Global 1s → 3d transition areas for the protein samples, when compared to published ferrous model data, indicate that the iron-ligand geometry in frataxin is highly symmetric, on the basis of the low values obtained compared to the value of 5.18 ±

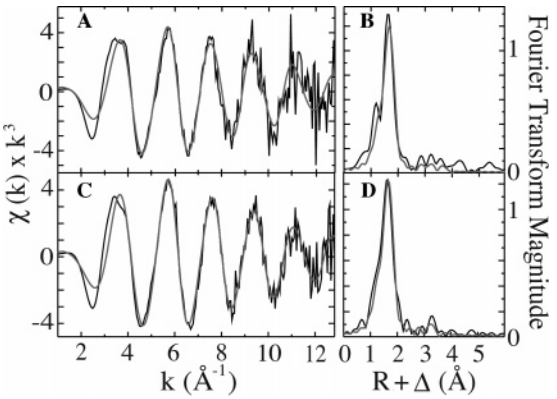

FIGURE 5: EXAFS and Fourier transforms of iron-loaded yeast frataxin XAS data. EXAFS spectra in black for yeast frataxin with one iron bound (A) and two iron bound (C), along with the corresponding Fourier transforms (B and D, respectively). Simulations for EXAFS and FT data are shown in gray.

0.015 from the highly symmetric $[Fe(H_2O)_6](NH_4)_2(SO_4)_2$ octahedral sample (*44*, *46*). Our XANES analysis therefore confirms that iron bound to monomeric yeast frataxin is high-spin and that ferrous iron is coordinated in a highly symmetric metal−ligand geometry, regardless of the metal/protein stoichiometry when up to two iron atoms are bound.

The protein EXAFS data were used to provide the metal−ligand geometric parameters for one and two ferrous iron bound to monomeric yeast frataxin. Raw EXAFS data for both 1Fe−Yfh1 and 2Fe−Yfh1 show a single frequency pattern with maximum amplitude at 5.5 $Å^{-1}$, suggesting symmetric Fe−nearest neighbor coordination geometry constructed by oxygen- and/or nitrogen-based ligands (black lines in parts A and C of Figure 5, respectively). The first large oscillation in both raw EXAFS data sets show a "camel-back" feature that is often attributed to imidazole scattering from histidine coordination to the metal (*49*). Fourier transforms of the EXAFS data show that a predominate ligand environment is localized in a symmetric pattern at a phase-shifted bond length ($R + \Delta$) of ca. 1.8 Å in both samples (parts B and D of Figure 5). Minimal long-range scattering (above 2.5 Å) is observed in both spectra. Spectral simulations show that ligands directly coordinated to the iron are completely oxygen/nitrogen-based (Table 1). In both 1Fe−Yfh1 and 2Fe−Yfh1 data sets, the nearest neighbor environment is best fit with a single nearest neighbor Fe−oxygen/nitrogen ligand environment that is partially disordered and with coordination numbers close to six (Figure 5, simulations in gray). These data indicate that iron bound to yeast frataxin is in a fairly symmetric Fe−(oxygen and/or nitrogen) ligand environment that is most likely six-coordinate. There is no evidence for Fe−S ligation, consistent with that fact that only amino acids with side-chain carboxylates and histidines were identified as residues perturbed in our NMR iron/protein titration. Furthermore, long-range scattering can only be fit with carbon scattering; thus, there is no evidence for any Fe···Fe scattering in either reduced iron sample. Finally, a comparison of the 1:1 and 2:1 Fe/protein data indicates that there is no major structural rearrangement at the metal center upon the addition of the second protein-bound iron atom.

DISCUSSION

The goal of this paper was to help characterize the structural and electronic properties of iron bound to monomeric yeast frataxin. Frataxin has been suggested to play a variety of roles in helping to maintain cellular iron homeostasis, most of which involve direct binding to iron. Frataxin facilitates in vivo heme and Fe−S cluster production, and the monomeric protein binds to enzyme partners that complete the assembly of these iron-containing cofactors, suggesting that monomeric protein may play a direct role in both processes by acting as the iron chaperone (*14*−*24*). Fluctuations in mitochondrial iron or Fe−cofactor levels and the differences in binding affinities between partners have been proposed to serve as the trigger for which assembly pathway is delivered iron (*23*). Frataxin has also been shown to oligomerize in vitro in high iron conditions, and the formation of these oligomers is highly dependent upon the solution ionic strength (*10*, *27*). Given that magnesium and calcium salts stabilize iron-loaded frataxin monomers, it has also been suggested that changes in mitochondrial ion concentrations may trigger frataxin to shift from an iron delivery to iron storage capacity (*27*). During the process of the iron-induced oligomerization of frataxin, while the trimeric protein appears to be the nucleating species for higher order assembly (*10*−*12*), it is surely the initial interaction of soluble monomeric protein with iron that instigates trimer formation. In addition, iron bound to frataxin multimers is predominately bound in a multinuclear form, while that bound to monomeric frataxin under low oxygen conditions appears to be as isolated atoms (*13*, *50*). Because a single iron atom is transferred during heme and Fe−S cluster assembly, it seems further unlikely that frataxin oligomers would participate as the source of metal during delivery. Given this rationale, having a structural and biochemical understanding of iron bound to monomeric

Table 1: Summary of EXAFS Fitting Results for Iron-Loaded Monomeric Yeast Frataxin[a]

	ligand environment[b]				ligand environment[b]				ligand environment[b]				
sample/fit number	atom[c]	R (Å)[d]	CN[e]	σ^2 [f]	atom[c]	R (Å)[d]	CN[e]	σ^2 [f]	atom[c]	R (Å)[d]	CN[e]	σ^2 [f]	F' [g]
1Fe−Yfh1 1[h]	O/N	2.12	4.75	5.80									0.98
2[h]	O/N	2.12	4.75	5.79	C	3.06	1	2.46					0.95
3[h]	O/N	2.12	4.75	5.78	C	3.07	1.75	4.30	C	3.30	1.25	4.47	0.92
2Fe−Yfh1 1[h]	O/N	2.12	5.25	5.72									0.54
2[h]	O/N	2.12	5.25	5.71	C	3.36	1	3.93					0.52
3[h]	O/N	2.12	5.25	5.72	C	3.00	1	3.49	C	3.42	1.25	2.82	0.50

[a] Data fit over a k range of 1−12.85 $Å^{-1}$. Values are averaged from at least two independent samples. [b] Independent metal−ligand scattering environment. [c] Scattering atoms: O (oxygen), N (nitrogen), and C (carbon). [d] Metal−ligand bond length. [e] Metal−ligand coordination number. [f] Debye−Waller factor in $Å^2 \times 10^3$. [g] Number of degrees of freedom weighted mean-square deviation between the data and fit. [h] Fit using only single-scattering Feff 7 theoretical models.

frataxin would help propel the general understanding of how frataxin functions toward controlling iron bioavailability in the cell.

The metal-binding affinity of frataxin is similar to those seen for the copper chaperones, suggesting a common theme in cellular metal delivery if frataxin is in fact acting as an iron chaperone. The micromolar dissociation constants measured for yeast frataxin, with respect to ferrous iron (K_d values of 2.0 and 3.0 μM), resemble those obtained for the human and bacterial orthologues (K_d values of 55.0 and 3.8 μM, respectively) (*22*, *51*). A comparison of the frataxin iron dissociation constants to those measured for the copper chaperones Cox17 and Atox1 (K_d values of ca. 0.17 and 10 μM, respectively) places these proteins within roughly the same affinity range (*52*, *53*). Ferrous iron-binding affinities measured for ferrochelatase are also within the micromolar range, indicating that the metal-binding affinity of frataxin is closely matched to protein partners that receive metal (*54*). It is therefore reasonable to suggest that frataxin can act as an iron chaperone during Fe−cofactor production. Given the high-binding affinity between frataxin and its protein-binding partners ferrochelatase and ISU (K_d values in the nanomolar range), it is also reasonable to suggest that, although frataxin binds ferrous iron weakly, regulation of metal-transfer events could be driven by the high affinity for forming a multiprotein complex (*14*, *22*, *23*). A general question is, given that cellular iron regulation is so tightly controlled and that mitochondrial free iron levels are surely below the micromolar range, why would cells utilize such a weak metal chaperone to help control the production of these essential iron−cofactors, especially given the high reactivity of the metal?

Metal-binding site(s) on monomeric frataxin must accommodate the binding of multiple iron atoms. Recent spectroscopic studies indicate that frataxin residues within the conserved acidic region at helix-1 and strand-1 are affected by iron binding (*28*, *32*, *51*). In these studies, NMR spectroscopy proved to be a sensitive tool for probing which frataxin amino acids are affected by the presence of bound ferrous iron. Iron titrations in yeast, human, and bacterial frataxin consistently show that residues within this conserved acidic region have their amide chemical shifts perturbed in the presence of iron. In organic buffers, all three frataxin orthologues also show a set of residues that have their amide resonances line-broadened beyond identification when protein is in the presence of the paramagnetic metal. Our original NMR iron titration in yeast frataxin showed no amide line broadening, suggesting that phosphate buffer can somehow alter iron binding to the protein or that iron binding is transient under those conditions (*28*). While amide chemical-shift perturbations may indicate a variety of occurrences (metal binding, localized change in the fold of the protein, changes in the chemical nature of the residue environment, etc.), it has been shown that protons located within a 10 Å radius of the bound paramagnetic metal can have their NMR line widths significantly broadened (*55*). Therefore, frataxin residues with acidic side chains that undergo significant amide line broadening in the presence of ferrous iron are most likely the amino acids in closer proximity to the metal, as compared to the residues that have only amide resonance chemical-shift changes. Therefore, the broadened residues are more likely the amino acids that act as ligands to the metal.

A comparison of the amide NMR resonances significantly line broadened in the presence of iron show that a subset of these residues are well-conserved. Amide resonances for yeast frataxin D31 and D35, corresponding to human residues D104 and E108 and bacterial residues L15 and E19, are significantly broadened in the human and yeast orthologues and, in the case of residue E19, in the bacterial orthologue (this paper and ref *32*). Acidic residues have side chain carboxylate groups that are often found to serve as iron ligands within metalloproteins (*33*, *34*, *56*, *57*). In all three cases, additional residues in close proximity to the acidic residues listed above are also broadened, suggesting that, if metal binds directly to their carboxylate side chain, the additional residues in close proximity should also be affected. In yeast frataxin, additional amide line-broadened residues in proximity to D31 and D35 include D28 and H32. Interestingly, yeast frataxin residues D28 and D31 have been shown to be required for the formation of the ferroxidase center observed in yeast frataxin oligomers by the Isaya laboratory, while D35 was implicated by the Craig group as assisting homo-oligomer formation and by the Isaya group for assisting in iron binding (*25*, *26*). In the bacterial and human orthologues, residues C-terminal to D35 in yeast frataxin are also broadened (*32*); these residues in yeast frataxin are simply perturbed in their amide chemical-shift values. These differences between papers may suggest that human and bacterial orthologues have a more expansive iron-binding surface on their helix-1 region or that the divalent magnesium ions that we used to stabilize the yeast protein as a monomer could be blocking weak transient metal-binding sites identified on the other orthologues. Yeast frataxin contains a second region of multiple residues that are line-broadened at their amide position in the presence of iron; this site includes residues E52 and E61 on the β-sheet surface of the protein. In this case, the broadened signals are not observed in the bacterial and human orthologues and only E52 is conserved. Interestingly, D50 in yeast frataxin is completely conserved, and this amide signal is broadened in both the human and bacterial orthologues, suggesting again that the β-sheet region of all frataxins acts as an additional metal-binding site on the protein on the opposite side of the helix-1 region of the molecule (*32*).

XAS studies of ferrous iron-bound yeast frataxin are consistent with a metal−ligand environment constructed by residues that were broadened in our NMR studies. Our XANES analysis indicates, on the basis of the first inflection point analysis of the iron edges, that iron is stable in the ferrous state when iron-loaded frataxin is kept anaerobic. Given that oxygen levels in the mitochondria are highly controlled, we suggest that the environment within the mitochondria may, under normal conditions, resemble the in vitro conditions that we report in our anaerobic studies. The 1s $\rightarrow$ 3d features indicate that ferrous iron bound to frataxin is high-spin and held within a coordination geometry that is nearly octahedral in its metal−ligand geometric symmetry. There are minimal differences in the edges when the protein has one or two metals bound, indicating that the two metal-binding sites on frataxin are either very similar (as expected because both appear to be constructed by acidic residues) or that, at the stoichiometric metal/protein concen-

tration, the two sites are being evenly populated (consistent with the very similar binding constants). EXAFS analysis confirms that ferrous iron bound to frataxin is coordinated by six oxygen/nitrogen based ligands. The metal−ligand nearest neighbor coordination environments in frataxin are nearly identical, independent of whether or not there are one or two metals bound. The predominate ligand-scattering environment is constructed of approximately six metal ligands at 2.12 Å. Analysis of the metal−ligand coordination environments for six-coordinate ferrous iron models in the Cambridge Structural Database (CSD) suggest that average $Fe^{II}-O_6$ distances from oxygens that are either protonated (resembling water) or in a carboxylate-like environment (representing Asp and Glu side-chain ligands) are 2.11 and 2.15 Å, respectively (*58*). Distances obtained in the 2.12 Å average iron−nearest neighbor environment of iron bound to frataxin closely match these six-coordinate model values, indicating that the majority of the protein-bound iron ligands most likely originate from acidic residue carboxylate side chains, water, or more likely a combination of both. In addition, the long-range (>2.5 Å) scattering observed in the Fourier transforms of the protein iron EXAFS would certainly be consistent with carboxylate carbon atom scattering. Interestingly, the appearance of the imidazole camelback feature in the first bead pattern of the protein EXAFS data suggests that there may be direct ligation of a histidine to the bound iron. The presence of long-range scattering features in our protein data could also be suggestive of Fe−imidazole scattering. In our NMR analysis, we identified H32 as a possible ligand that is directly coordinated to iron. Scattering from H32 could contribute to the apparent imidazole EXAFS scattering that we see in our data, although an equally likely scenario exists that the apparent imidazole scattering actually may come from carboxylate carbon scattering. Additional experiments are underway to test if H32 directly binds iron. There is no evidence in our reduced samples of the Fe···Fe scattering observed in ferric-loaded frataxin oligomers, and the general Fe−O bond distance in our monomeric samples is longer than those reported in the oligomer study, as expected given the difference in the metal oxidation state (*13*). These data suggest that, under reducing conditions, iron bound to monomeric frataxin does not exist in a ferrihydrite form, although the absence of an Fe···Fe signal does not rule out the possibility that the two bound metals in the 2Fe−Yfh1 sample are not in close proximity to each other (*35*, *59*).

On the basis of the paramagnetically broadened residues in the NMR titrations and on the geometric parameters obtained in our XAS studies, our results are consistent with yeast frataxin having two unique iron-binding regions. The first site involves side chains from residues D28, D31, H32, and D35 on helix-1 of the protein (Figure 6A). At this site, only the acidic residues are conserved, while the histidine is a serine in the human protein. This first site is close to the additional conserved acidic residues, C-terminal but still on helix-1 in position, which are affected by the presence of iron. The second site may involve residues E52 and E61 on the β-sheet surface of the molecule, possibly also including D50, a residue that is consistently broadened in the human and bacterial NMR iron titrations and shifted in our Yfh1 iron/phosphate buffer titration (Figure 6B). The fact that these two unique sites are located on distant and opposite regions

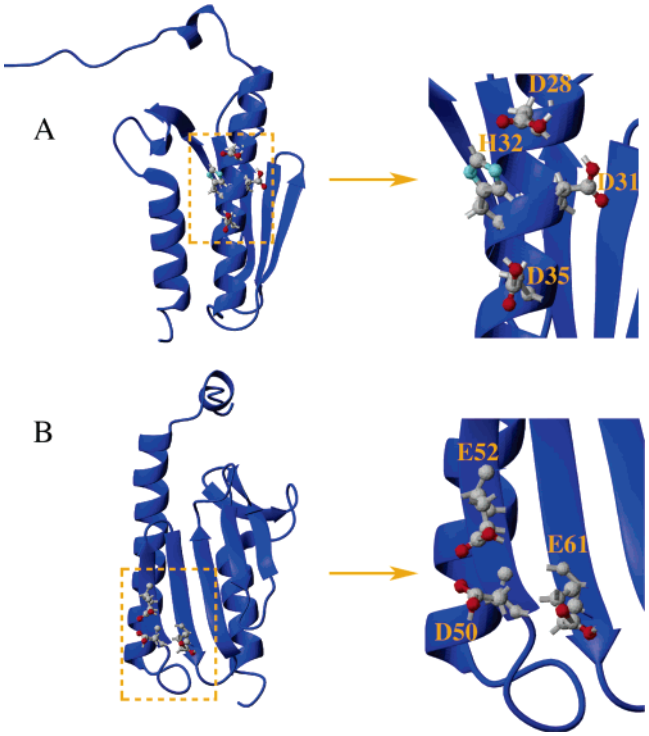

FIGURE 6: Location of yeast frataxin residues strongly perturbed by the presence of iron. (A) Apoprotein structure with helix-1 amino acid side chain atoms from line-broadened amide resonances in the yeast frataxin NMR iron titration. Expanded view to the right of arrows. (B) Apoprotein structure with β-sheet amino acid side chain atoms from line-broadened amide resonances in the yeast frataxin NMR iron titration and D50. Expanded view to the right of the arrow. Note: the structure of the protein represents an updated PDB file for yeast frataxin (PDB accession number 2GA5), currently available for download.

of the frataxin structure may indicate that each could be selectively responsible for iron delivery to a different protein-binding partner. In vivo and in vitro studies are currently underway to dissect the role of each site in the different proposed iron delivery function of frataxin.

Additional conserved acidic helix-1 residues C-terminal to amino acids that construct our first proposed metal-binding site are also affected by the presence of iron in the NMR titrations and line broadened in the bacterial and human studies (*32*). Interestingly, human frataxin has been shown to bind six iron atoms, while the bacterial homologue binds two iron atoms in the micromolar range, with multiple additional residues at an even weaker (unmeasurable by ITC) binding affinity (*22*, *23*, *32*). We believe these additional helix-1 residues C-terminal to those identified in the first binding site (including yeast frataxin residues E38, E39, and E42 shifted in our iron titration) may construct a possible third (but transient) binding site for additional metals during aerobic/iron overloaded conditions. These acidic conserved helix-1 residues are substantially broadened in the human and bacterial iron NMR titrations, and E38, E39, and E42 have been shown to be important for iron binding and the ferroxidase chemistry noted in yeast frataxin oligomers (*25*). In our yeast iron-binding analysis, this site may also be a transient site for weaker binding salt divalent ions (i.e., Mg^{2+}, which we have in abundance in our samples), and when these salts are in high abundance, they out-compete iron for binding.

In summary, all three structurally characterized frataxin orthologues bind multiple iron atoms with a micromolar-binding affinity when the protein exists in the monomeric state, consistent with a functional role of the monomeric protein being involved in iron binding and delivery. N-Terminally conserved acidic residues spanning the helix-1 and strand-1 regions of the protein are significantly perturbed in their chemical environments upon binding of paramagnetic iron, implicating that residues in these regions are performing selective iron binding. Ferrous iron bound to monomeric frataxin is high-spin and coordinated in a highly symmetric metal−ligand geometry constructed of only oxygen and nitrogen ligands. These ligands are presumably donated from carboxylate- and imidazole-containing amino acid side chains and from coordinated water molecules. The weak nature of the metal-binding affinity of the protein and the ligand environment utilized by the protein to bind metal would be consistent with frataxin acting as an iron chaperone; the protein must be able to form a favorable interface with its protein partners and also easily release the metal. The iron-binding helix-1 and strand-1 regions of frataxin have already been implicated in helping form the intermolecular interface when the protein binds to ferrochelatase (*28*, *60*) and ISU (unpublished results). Additional structural characterization will be critical to help elucidate how frataxin binds iron and docks with its protein partners to promote metal delivery.

ACKNOWLEDGMENT

Portions of this research were carried out at both the Stanford Synchrotron Radiation Laboratory (SSRL) and the National Synchrotron Light Source (NSLS). SSRL is a national user facility operated by Stanford University on behalf of the U.S. Department of Energy, Office of Basic Energy Sciences. The SSRL Structural Molecular Biology Program is supported by the Department of Energy, Office of Biological and Environmental Research, and by the NIH, National Center for Research Resources, Biomedical Technology Program. NSLS, located at Brookhaven National Laboratory, is supported by the U.S. Department of Energy, Division of Materials Sciences and Division of Chemical Sciences, under contract number DE-AC02-98CH10886.

REFERENCES

1. Skre, H. (1975) Friedreich's ataxia in western Norway, *Clin. Genet 7*, 287−298.
2. Winter, R. M., Harding, A. E., Baraitser, M., and Bravery, M. B. (1981) Intrafamilial correlation in Friedreich's ataxia, *Clin. Genet. 20*, 419−427.
3. Pandolfo, M., Sirugo, G., Antonelli, A., Weitnauer, L., Ferretti, L., Leone, M., Dones, I., Cerino, A., Fujita, R., Hanauer, A., et al. (1990) Friedreich ataxia in Italian families: Genetic homogeneity and linkage disequilibrium with the marker loci D9S5 and D9S15, *Am. J. Hum. Genet. 47*, 228−235.
4. Campuzano, V., Montermini, L., Molto, M. D., Pianese, L., Cossee, M., Cavalcanti, F., Monros, E., Rodius, F., Duclos, F., Monticelli, A., Zara, F., Canizares, J., Koutnikova, H., Bidichandani, S. I., Gellera, C., Brice, A., Trouillas, P., de Michele, G., Filla, A., de Frutos, R., Palau, F., Patel, P. I., di Donato, S., Mandel, J. L., Cocozza, S., Koenig, M., and Pandolfo, M. (1996) Friedreich's ataxia: Autosomal recessive disease caused by an intronic GAA triplet repeat expansion, *Science 271*, 1423−1427.
5. Koutnikova, H., Campuzano, V., Foury, F., Dolle, P., Cazzalini, O., and Koenig, M. (1997) Studies of human, mouse and yeast homologues indicate a mitochondrial function for frataxin, *Nat. Genet. 16*, 345−351.
6. Radisky, D. C., Babcock, M. C., and Kaplan, J. (1999) The yeast frataxin homologue mediates mitochondrial iron efflux: Evidence for a mitochondrial iron cycle, *J. Biol. Chem. 274*, 4497−4499.
7. Ristow, M., Pfister, M. F., Yee, A. J., Schubert, M., Michael, L., Zhang, C. Y., Ueki, K., Michael, M. D., II, Lowell, B. B., and Kahn, C. R. (2000) Frataxin activates mitochondrial energy conversion and oxidative phosphorylation, *Proc. Natl. Acad. Sci. U.S.A. 97*, 12239−12243.
8. Bulteau, A. L., O'Neill, H. A., Kennedy, M. C., Ikeda-Saito, M., Isaya, G., and Szweda, L. I. (2004) Frataxin acts as an iron chaperone protein to modulate mitochondrial aconitase activity, *Science 305*, 242−245.
9. Bulteau, A. L., Lundberg, K. C., Ikeda-Saito, M., Isaya, G., and Szweda, L. I. (2005) Reversible redox-dependent modulation of mitochondrial aconitase and proteolytic activity during in vivo cardiac ischemia/reperfusion, *Proc. Natl. Acad. Sci. U.S.A. 102*, 5987−5991.
10. Adamec, J., Rusnak, F., Owen, W. G., Naylor, S., Benson, L. M., Gacy, A. M., and Isaya, G. (2000) Iron-dependent self-assembly of recombinant yeast frataxin: Implications for Friedreich ataxia, *Am. J. Hum. Genet. 67*, 549−562.
11. Cavadini, P., O'Neill, H. A., Benada, O., and Isaya, G. (2002) Assembly and iron-binding properties of human frataxin, the protein deficient in Friedreich ataxia, *Hum. Mol. Genet. 11*, 217−227.
12. Gakh, O., Adamec, J., Gacy, A. M., Twesten, R. D., Owen, W. G., and Isaya, G. (2002) Physical evidence that yeast frataxin is an iron storage protein, *Biochemistry 41*, 6798−6804.
13. Nichol, H., Gakh, O., O'Neill, H. A., Pickering, I. J., Isaya, G., and George, G. N. (2003) Structure of frataxin iron cores: An X-ray absorption spectroscopic study, *Biochemistry 42*, 5971−5976.
14. Lesuisse, E., Santos, R., Matzanke, B. F., Knight, S. A., Camadro, J. M., and Dancis, A. (2003) Iron use for haeme synthesis is under control of the yeast frataxin homologue (Yfh1), *Hum. Mol. Genet. 12*, 879−889.
15. Schoenfeld, R. A., Napoli, E., Wong, A., Zhan, S., Reutenauer, L., Morin, D., Buckpitt, A. R., Taroni, F., Lonnerdal, B., Ristow, M., Puccio, H., and Cortopassi, G. A. (2005) Frataxin deficiency alters heme pathway transcripts and decreases mitochondrial heme metabolites in mammalian cells, *Hum. Mol. Genet. 14*, 3787−3799.
16. Zhang, Y., Lyver, E. R., Knight, S. A., Lesuisse, E., and Dancis, A. (2005) Frataxin and mitochondrial carrier proteins, Mrs3p and Mrs4p, cooperate in providing iron for heme synthesis, *J. Biol. Chem. 280*, 19794−19807.
17. Gerber, J., Muhlenhoff, U., and Lill, R. (2003) An interaction between frataxin and Isu1/Nfs1 that is crucial for Fe/S cluster synthesis on Isu1, *EMBO Rep. 4*, 906−911.
18. Stehling, O., Elsasser, H. P., Bruckel, B., Muhlenhoff, U., and Lill, R. (2004) Iron−sulfur protein maturation in human cells: Evidence for a function of frataxin, *Hum. Mol. Genet. 13*, 3007−3015.
19. Muhlenhoff, U., Gerber, J., Richhardt, N., and Lill, R. (2003) Components involved in assembly and dislocation of iron−sulfur clusters on the scaffold protein Isu1p, *EMBO J. 22*, 4815−4825.
20. Muhlenhoff, U., Richhardt, N., Ristow, M., Kispal, G., and Lill, R. (2002) The yeast frataxin homolog Yfh1p plays a specific role in the maturation of cellular Fe/S proteins, *Hum. Mol. Genet. 11*, 2025−2036.
21. Ramazzotti, A., Vanmansart, V., and Foury, F. (2004) Mitochondrial functional interactions between frataxin and Isu1p, the iron−sulfur cluster scaffold protein, in *Saccharomyces cerevisiae*, *FEBS Lett. 557*, 215−220.
22. Yoon, T., and Cowan, J. A. (2003) Iron−sulfur cluster biosynthesis. Characterization of frataxin as an iron donor for assembly of [2Fe−2S] clusters in ISU-type proteins, *J. Am. Chem. Soc. 125*, 6078−6084.
23. Yoon, T., and Cowan, J. A. (2004) Frataxin-mediated iron delivery to ferrochelatase in the final step of heme biosynthesis, *J. Biol. Chem. 279*, 25943−25946.
24. Park, S., Gakh, O., O'Neill, H. A., Mangravita, A., Nichol, H., Ferreira, G. C., and Isaya, G. (2003) Yeast frataxin sequentially chaperones and stores iron by coupling protein assembly with iron oxidation, *J. Biol. Chem. 278*, 31340−31351.
25. Gakh, O., Park, S., Liu, G., Macomber, L., Imlay, J. A., Ferreira, G. C., and Isaya, G. (2006) Mitochondrial iron detoxification is a primary function of frataxin that limits oxidative damage and preserves cell longevity, *Hum. Mol. Genet. 15*, 467−479.

26. Aloria, K., Schilke, B., Andrew, A., and Craig, E. A. (2004) Iron-induced oligomerization of yeast frataxin homologue Yfh1 is dispensable in vivo, *EMBO Rep. 5*, 1096−1101.
27. Adinolfi, S., Trifuoggi, M., Politou, A. S., Martin, S., and Pastore, A. (2002) A structural approach to understanding the iron-binding properties of phylogenetically different frataxins, *Hum. Mol. Genet. 11*, 1865−1877.
28. He, Y., Alam, S. L., Proteasa, S. V., Zhang, Y., Lesuisse, E., Dancis, A., and Stemmler, T. L. (2004) Yeast frataxin solution structure, iron binding, and ferrochelatase interaction, *Biochemistry 43*, 16254−16262.
29. Musco, G., Stier, G., Kolmerer, B., Adinolfi, S., Martin, S., Frenkiel, T., Gibson, T., and Pastore, A. (2000) Towards a structural understanding of Friedreich's ataxia: The solution structure of frataxin, *Structure 8*, 695−707.
30. Dhe-Paganon, S., Shigeta, R., Chi, Y. I., Ristow, M., and Shoelson, S. E. (2000) Crystal structure of human frataxin, *J. Biol. Chem. 275*, 30753−30756.
31. Cho, S. J., Lee, M. G., Yang, J. K., Lee, J. Y., Song, H. K., and Suh, S. W. (2000) Crystal structure of *Escherichia coli* CyaY protein reveals a previously unidentified fold for the evolutionarily conserved frataxin family, *Proc. Natl. Acad. Sci. U.S.A. 97*, 8932−8937.
32. Nair, M., Adinolfi, S., Pastore, C., Kelly, G., Temussi, P., and Pastore, A. (2004) Solution structure of the bacterial frataxin ortholog, CyaY: Mapping the iron binding sites, *Structure 12*, 2037−2048.
33. Rosenzweig, A. C., Frederick, C. A., Lippard, S. J., and Nordlund, P. (1993) Crystal structure of a bacterial non-haem iron hydroxylase that catalyses the biological oxidation of methane, *Nature 366*, 537−543.
34. Nordlund, P., and Eklund, H. (1993) Structure and function of the *Escherichia coli* ribonucleotide reductase protein R2, *J. Mol. Biol. 232*, 123−164.
35. Riggs-Gelasco, P. J., Stemmler, T. L., and Penner-Hahn, J. E. (1995) XAFS of dinuclear metal sites in proteins and model compounds, *Coord. Chem. Rev. 114*.
36. Mori, S., Abeygunawardana, C., O'Neil Johnson, M., and van Zijl, P. C. M. (1995) Improved sensitivity of HSQC spectra of exchanging protons at short interscan delays using a new fast HSQC (FHSQC) detection scheme that avoids water saturation, *J. Magn. Res. B 108*, 94−98.
37. Wishart, D. S., Bigam, C. G., Yao, J., Abildgaard, F., Dyson, H. J., Oldfield, L., Markley, J. L., and Sykes, B. D. (1995) ^{1}H, ^{13}C and ^{15}N chemical shift referencing in biomolecular NMR, *J. Biomol. NMR 6*, 135−140.
38. Delaglio, F., Grzesiek, S., Vuister, G. W., Zhu, G., Pfeifer, J., and Bax, A. (1995) NMRPipe: A multidimensional spectral processing system based on UNIX pipes, *J. Biomol. NMR 6*, 277−293.
39. Goddard, T. D., and Kneller, D. G. (2001) University of California, San Francisco, CA.
40. Grzesiek, S., Bax, A., Clore, G. M., Gronenborn, A. M., Hu, J. S., Kaufman, J., Palmer, I., Stahl, S. J., and Wingfield, P. T. (1996) The solution structure of HIV-1 Nef reveals an unexpected fold and permits delineation of the binding surface for the SH3 domain of Hck tyrosine protein kinase, *Nat. Struct. Biol. 3*, 340−345.
41. Garrett, T. P. J., Guss, J. M., and Freeman, H. C. (1983) Hexakis-(imidazole)manganese(II) dichloride tetrahydrate, $[Mn(C_3H_4N_2)_6]$-$Cl_2 \cdot 4H_2O$ and hexakis(imidazole)zinc(II) dichloride tetrahydrate, $[Zn(C_3H_4N_2)_6]Cl_2 \cdot 4H_2O$, *Acta Crystallogr., Sect. C: Cryst. Struct. Commun. 39*, 1027−1031.
42. Rehr, J. J., and Ankudinov, A. L. (2001) Progress and challenges in the theory and interpretation of X-ray spectra, *J. Synchrotron Radiat. 8*, 61−65.
43. George, G. N., George, S. J., and Pickering, I. J. (2001) http://www-ssrl.slac.stanford.edu/~george/exafspak/exafs.htm.
44. Westre, T. E., Kennepohl, P., DeWitt, J. G., Hedman, B., Hodgson, K. O., and Solomon, E. I. (1997) A multiplet analysis of the Fe K-edge 1s → 3d pre-edge features of iron complexes, *J. Am. Chem. Soc. 119*, 6297−6314.
45. Lee, P. A., Citrin, P. H., Eisenberger, P., and Kincaid, B. M. (1981) Extended X-ray absorption fine structure—Its strengths and limitations as a structural tool, *Rev. Mod. Phys. 53*, 769−806.
46. Randall, C. R., Shu, L., Chiou, Y.-M., Hagen, K. S., Ito, M., Kitajima, N., Lachicotte, R. J., Zang, Y., and Que, L., Jr. (1995) X-ray absorption pre-edge studies of high-spin iron(II) compounds, *Inorg. Chem. 34*, 1036−1039.
47. Roe, A. L., Schneider, D. J., Mayer, R. L., Pyrz, J. W., Widon, J., and Que, L., Jr. (1984) X-ray absorption spectroscopy of iron−tyrosinate proteins, *J. Am. Chem. Soc. 106*, 1676−1681.
48. Shulman, R. G., Yafet, Y., Eisenberger, P., and Blumberg, W. E. (1976) Observation and interpretation of X-ray absorption edges in iron compounds and proteins, *Proc. Natl. Acad. Sci. U.S.A. 73*, 1384−1388.
49. Feiters, M. C., Navaratnam, S., Al-Hakim, M., Allen, J. C., Spek, A. L., Veldink, G. A., and Vliegenthart, J. F. G. (1988) EXAFS of polu[*m*-hexakis(2-methylimidazolato-*N*,*N*′)triiron(II)]: Implications for metalloprotein studies, *J. Am. Chem. Soc 110*, 7746−7750.
50. Park, S., Gakh, O., Mooney, S. M., and Isaya, G. (2002) The ferroxidase activity of yeast frataxin, *J. Biol. Chem 277*, 38589−38595.
51. Bou-Abdallah, F., Adinolfi, S., Pastore, A., Laue, T. M., and Dennis Chasteen, N. (2004) Iron binding and oxidation kinetics in frataxin CyaY of *Escherichia coli*, *J. Mol. Biol. 341*, 605−615.
52. Abajian, C., Yatsunyk, L. A., Ramirez, B. E., and Rosenzweig, A. C. (2004) Yeast cox17 solution structure and copper(I) binding, *J. Biol. Chem. 279*, 53584−53592.
53. Wernimont, A. K., Yatsunyk, L. A., and Rosenzweig, A. C. (2004) Binding of copper(I) by the Wilson disease protein and its copper chaperone, *J. Biol. Chem. 279*, 12269−12276.
54. Shi, Z., and Ferreira, G. C. (2003) A continuous anaerobic fluorimetric assay for ferrochelatase by monitoring porphyrin disappearance, *Anal. Biochem. 318*, 18−24.
55. La Mar, G. N., and de Ropp, J. S. (1993) NMR methodology for paramagnetic proteins, in *Biological Magnetic Resonance* (Berliner, L. J., and Reuben, J., Eds.) pp 1−73, Plenum Press, New York.
56. Holmes, M. A., and Stenkamp, R. E. (1991) Structures of met and azidomet hemerythrin at 1.66 Å resolution, *J. Mol. Biol. 220*, 723−737.
57. Holmes, M. A., Le Trong, I., Turley, S., Sieker, L. C., and Stenkamp, R. E. (1991) Structures of deoxy and oxy hemerythrin at 2.0 Å resolution, *J. Mol. Biol. 218*, 583−593.
58. Centre, C. C. D. (2002) Cambridge.
59. Stemmler, T. L., Sossong, T. M., Jr., Goldstein, J. I., Ash, D. E., Elgren, T. E., Kurtz, D. M., Jr., Penner-Hahn, J. E. (1997) EXAFS comparison of the dimanganese core structures of manganese catalase, arginase and manganese-substituted ribonucleotide reductase and hemerythrin, *Biochemistry 36*, 9847−9858.
60. Bencze, K. Z., Yoon, T., Bradley, P. B., Cowan, J. A., and Stemmler, T. L. (2006) Human frataxin: Iron structure and ferrochelatase binding surface, *J. Am. Chem. Soc.*, manuscript submitted.

BI060424R